Geophys. J. Int. (2008) **175,** 1095–1107 doi: 10.1111/j.1365-246X.2008.03929.x

Velocities and driving pressures of clay-rich sediments injected into clastic dykes during earthquakes

Tsafrir Levi,[1,2] Ram Weinberger,[1] Yehuda Eyal,[2] Vladimir Lyakhovsky[1] and Eyal Heifetz[3]

[1] *Geological Survey of Israel,* 30 *Malkhe Israel, Jerusalem* 95501, *Israel*
[2] *Department of Geological and Environmental Sciences, Ben Gurion University of the Negev, Beer Sheva, Israel. E-mail: tafrir@gsi.ac.il*
[3] *Department of Geophysics and Planetary Sciences, Tel Aviv University, Tel Aviv* 69978, *Israel*

Accepted 2008 July 27. Received 2008 June 22; in original form 2007 May 15

SUMMARY

We studied the velocities and driving pressures associated with clastic-dyke formation in the Ami'az plain, where hundreds of clastic dykes cross-cut the soft rock of the late Pleistocene lacustrine Lisan Formation, within the seismically active Dead Sea basin. Flow of clastic material into fractures and opening of the fractures are two mechanisms that occur during earthquake-induced clastic dyke emplacement. Two analytic models were established, based on field observations and experimental viscosity tests, to estimate the velocities and driving pressures that were associated with dyke emplacement: (a) a channel flow for upward injection of a clay–water mixture and (b) a profile of fracture dilation based on the elastic theory analysis. The two models predict that pressures between 1 and 10 MPa are generated in the source layer and dykes in the last stage of the injection process. In addition, the channel flow model predicts that the injection velocity reaches metres to tens of metres per second and the emplacement time of the clastic dykes is on a scale of seconds. It is suggested that the high pressure values represent the static stress drop during earthquake events or represent dynamic stresses resulting from the seismic waves which passed through the soft lacustrine rocks. In both cases, the predicted high pressure values indicate that the clastic dyke was emplaced in close proximity of an active segment of the Dead Sea Fault during the late Pleistocene-Holocene.

Key words: Fracture and flow; Palaeoseismology; Mechanics, theory, and modelling.

1 INTRODUCTION

Clastic dykes are discordant, tabular bodies comprised of weakly to strongly lithified clastic detritus. They are formed either by passive deposition of clastic material within pre-existing or earthquake-induced tensile fissures or by dynamic fracturing associated with injection of clastic material during overpressure build-up. The latter structures, known as injection clastic dykes, are the focus of the present study and are considered an example of natural hydraulic fractures (Jolly & Lonergan 2002). Hundreds of clastic dykes are exposed in Ami'az Plain, Dead Sea basin (Fig. 1). Previous studies (Levi *et al*. 2006a,b) demonstrated that part of these clastic dykes, connected to a clay-rich layer of the Lisan Formation (Fig. 1) were formed by injection of material from that layer into the Lisan formation. In such intrusions, the particle-water mixture, which is injected under high-pressure into the surrounding host rock, requires a sustained pressure difference between the mixture in the source layer and the mixture in the propagating fracture. This pressure difference leads to dilation of the fracture and enables the particle-water mixture to flow through the fractures. Once the excess pressure decreases, fracture propagation terminates and the injection process stops.

Emplacement of clastic dykes might form during strong earthquakes (probably $M \geq 6.5$). Earthquake-induced clastic dykes have been used for locating palaeo-epicentres (e.g. Galli 2000 and references therein). Calculating the injection velocities and the pressures involved in the emplacement of clastic dyke may provide important information about the stress values generated during earthquakes.

Engineering studies of ground deformation associated with earthquakes have shown that near-surface granular porous material is liquefied by cyclic shear loading (Seed 1979; McCalpin 1996) or static stresses (e.g. Seed 1979) generated during earthquakes. The liquefaction occurs as a consequence of the increased pore-water pressure, whereby the granular porous material (i.e. sand) is transformed from a solid state into a fluid-like state. Soft sediment deFormation is referred to as flowage or fluidization of cohessionless clay-rich sediments during earthquakes (e.g. Mohindra & Bagati 1996; Rodríguez-Pascua *et al*. 2000; Moretti 2000). Behaviour of soft sediments under cyclic loading has been relatively less studied compared with those of sands. Accordingly, the criteria used to define the liquefaction of sand may no longer be applicable for clay-rich sediments (e.g. Yi lmaz *et al*. 2004 and references therein). The fluidization process of the clay-rich source layer, several metres below the surface is associated with a pressure build-up that causes

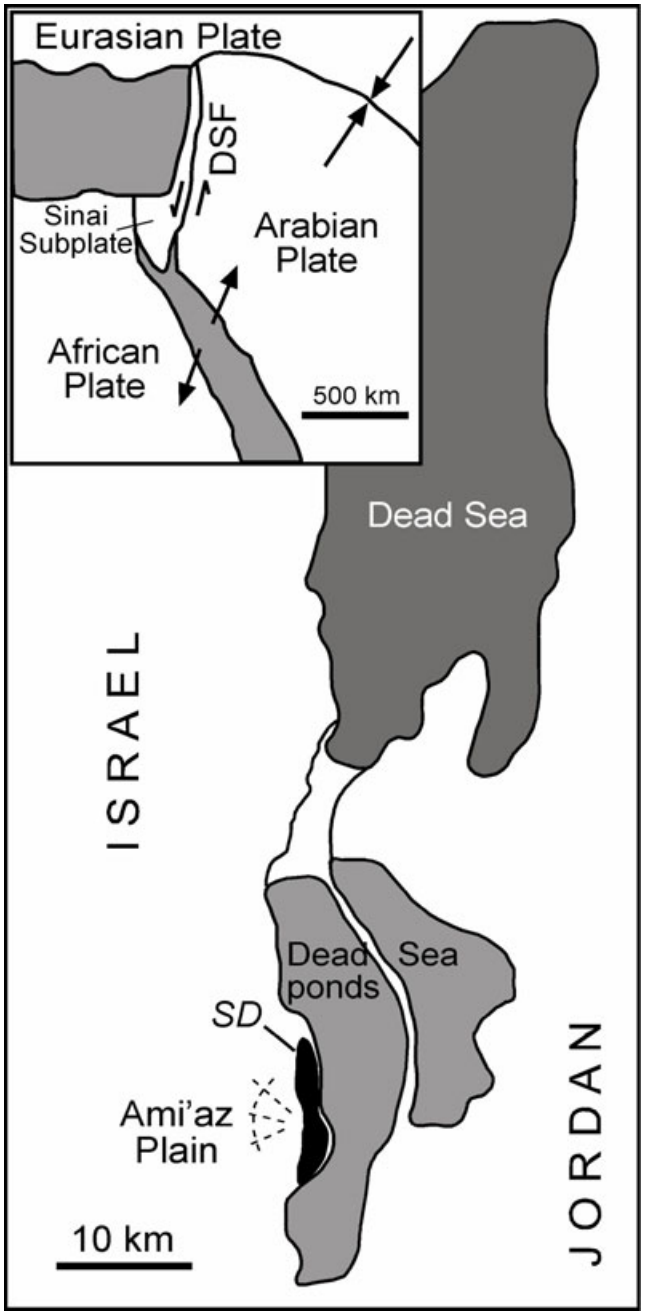

Figure 1. Location maps of the study area. The regional setting of the Dead Sea Fault (inset) and the Ami'az Plain with the clastic dykes marked schematically by dashed lines. DSF, Dead Sea Fault; SD, Sedom Diapir (after Levi *et al*. 2006a).

the particle-water mixture to be injected upwards. The background physics of this pressure build-up process and its relation to the dynamic stresses generated during earthquakes has been studied little and not completely understood (e.g. Melosh 1996; Bachrach *et al*. 2001).

In most cases, pressures and injection velocities that are generated during earthquakes and form structures, such as clastic dykes, cannot be directly monitored. There are relatively few quantitative studies of earthquake-induced structures (i.e. seismites), in general and that of clastic dykes, in particular. The pressure values that are estimated for dyke formation are generally of the order of several MPa. This estimation is based on the assumption that the formation was under lithostatic pressures corresponding to depths of tens to hundred of metres (e.g. Jolly & Lonergan 2002). Fluidized particle-water mixtures that have low viscosities are expected to flow under turbulence conditions (Turcotte & Schubert 1982).

In previous studies of clastic dykes in the Dead Sea basin Levi *et al.* (2006a,b) concluded that the dykes were emplaced during earthquake events. Field observations and anisotropy of magnetic susceptibility (AMS) analysis suggest that the fluidization process of the source material was dynamic and occurred simultaneously with the fracturing process. The AMS fabric analysed by Levi *et al*. (2006a,b) indicates that the flow was turbulent and, qualitatively, associated with high injection velocities of well-mixed, homogeneous fluid. The aim of this study is to quantify the velocity and the associated driving pressures that are involved during the last stage of the injection process. We developed two mechanical models for the emplacement of clastic dykes; one is based on the channel flow theory and the other on the elastic crack theory. For this quantification, we also experimentally measured the dynamic viscosities of the clay-water mixture under different flow rates. The obtained injection velocities and driving pressures shed light on the fluidization process and clastic dyke build-up during earthquakes.

2 GEOLOGIC SETTING

The Ami'az Plain study area (Fig. 1) is located west of the Mount Sedom salt diapir (Zak 1967; Weinberger *et al*. 2006a,b), near the southwestern margin of the Dead Sea basin and adjacent to the Dead Sea Fault, (e.g. Quennell 1959; Freund *et al*. 1968; Garfunkel 1981). The Dead Sea basin is a continental depression, which is bounded on the east and west by a series of oblique–normal faults. The Ami'az Plain is one of the downfaulted blocks developed within the depression.

The incision of Nahal (Wadi) Perazim in the Ami'az Plain exposes the entire Lisan section and about 250 large-scale (height, lenght > 10 m) clastic dykes, which cut through the section. Based on U–Th dating, the age of the Lisan Formation is between ∼70 000 and 15 000 yr B.P. (Haase-Schramm *et al*. 2004). The bedrock of the Ami'az Plain is the ∼40 m thick Late Pleistocene lacustrine Lisan Formation consisting mostly of authigenic (chalk) aragonite laminae, alternating with fine detritus layers (Begin *et al*. 1980). At the lower part of this formation, there are a few thick clay rich layers. Shaking and squeezing such wet clay layers causes a fast expulsion of pore water, a drastic loss of shear strength and consequent material flow and pressure build-up, which is not expected for the chalky host rock (Arkin & Michaeli 1986). The upper part of the Lisan Formation consists of a ∼1 m thick relatively stiff gypsum layer. A thin veneer (<1 m) of aeolian and fluvial sediments overlies the Lisan Formation and covers large parts of the plain.

The palaeoseismic record from the Dead Sea basin based on breccia layers reveals numerous moderate to strong earthquake events between 70 000 and 15 000 yr BP (e.g. Marco & Agnon 1995; Begin *et al*. 2005) and during the Holocene (Enzel *et al.* 2000; Ken-Tor *et al*. 2001; Begin *et al*. 2005). The strongest recorded event in the Dead Sea basin is the $M = 6.2$ earthquake of 1927 July 11; whose focal mechanism solution is a left-lateral motion (Ben-Menahem *et al*. 1976; Shapira *et al*. 1993). The strongest instrumentally recorded event along the Dead Sea Fault is the $M_w = 7.2$ 1995 November 22 Gulf of Aqaba earthquake (Hofstetter 2003).

Most of the clastic dykes in the Ami'az Plain are injection structures, which were induced by late Pleistocene-Holocene earthquakes along faults comprising the seismically active Dead Sea Fault (Levi *et al*. 2006a,b). The earthquake induced fluidization and injection of clastic material into dykes in the Ami'az Plain occurred, based on resetting of quartz Optically Stimulated Luminescence (OSL) signals, between 15 000 and 7 000 years BP (Porat *et al*. 2007).

The injection clastic dykes are composed of green clay, silty quartz and some aragonite fragments. The dyke heights vary between 5 mm and 18 m, the smallest of which (<0.5 m) are termed dykelets (Fig. 2b). The width (thickness) varies between 1 mm and 0.18 m, and length, between 5 mm and 100 m. The width of the large-scale dykes (>10 m) is generally greater than 7 mm. In several cases, the measured width at the lower parts of these dykes is smaller than 7 mm, and it is not clear if such a narrow width is kept constant along the entire height of the dykes.

A connection between a green clay-rich layer of the Lisan Formation and the dyke-fill, observed in several dykes, unequivocally indicates that the dykes were formed by injection of material from that layer. Levi *et al*. (2006a,b) discussed several arguments strongly indicating that the dykes, filled with the green clay-rich layer, are pressure-driven injected structures. The principal arguments are briefly summarized below:

(1) There is a physical connection between the source layers and clastic-dykes indicating upward transport of sediments during injection.

(2) There is a similar mineral assemblage, based on the interpretation of XRD, and magnetic measurements of the rock, in both the source layers and the respective dykes.

(3) The AMS analysis of the infill sediment shows a magnetic injection fabric compatible with injection flow and not with passive deposition of clastic material into pre-existing fissures.

(4) The geometric pattern of small dykelets and segments formed in the upper part of the section shows that the lateral direction of the dyke propagation coincides with the lateral flow direction detected by AMS analysis.

Dykes propagating below the source layer are terminated against alternating gypsum and aragonite laminae of the lower Lisan

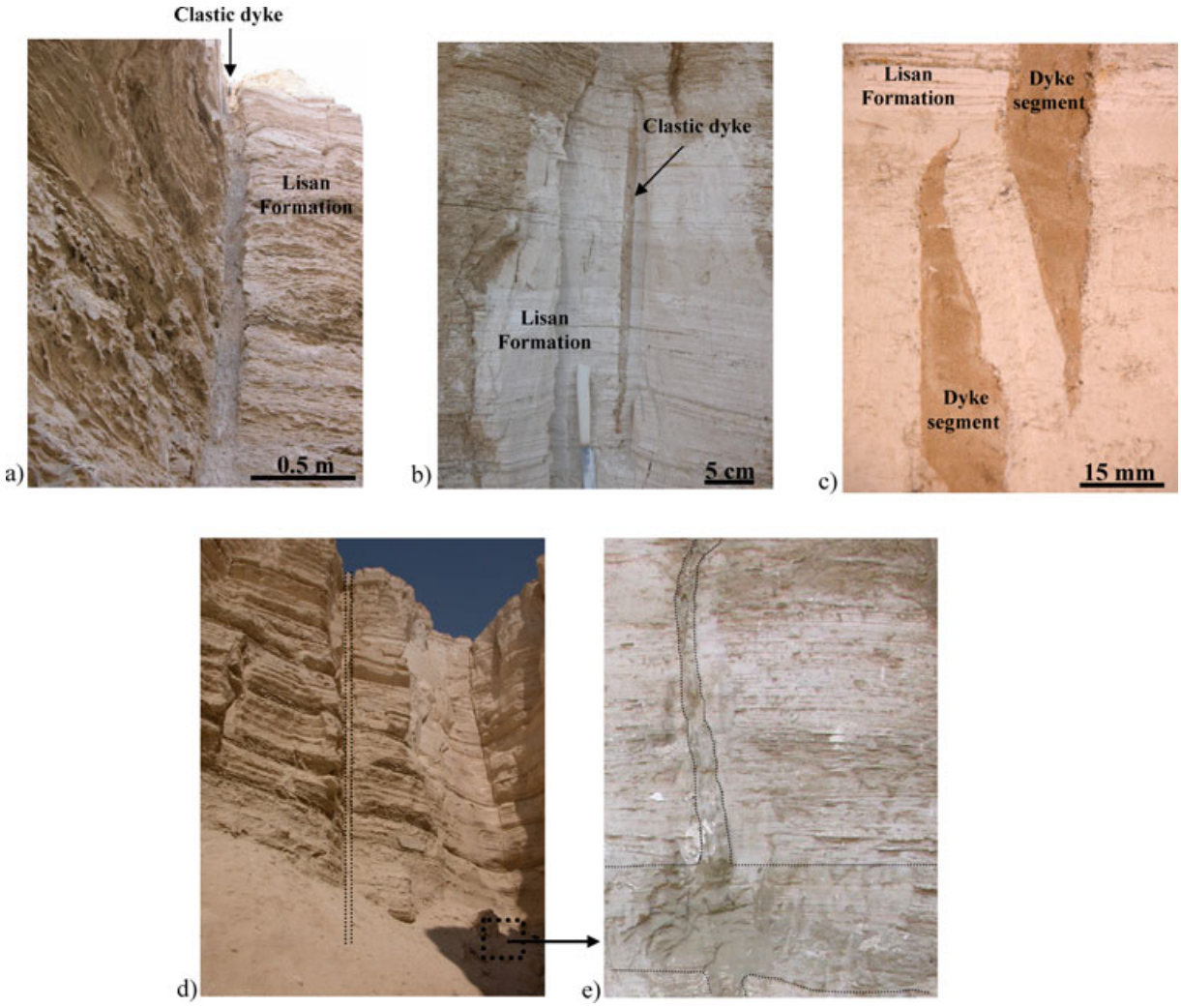

Figure 2. (a) Large-scale clastic, dyke about 18 m high, crossing the Lisan section. The dyke shape resembles a filled channel. (b) Small-scale clastic dyke (dykelet) at the upper part of the Lisan section. The dykelet has a quasi-elliptical shape. (c) Two overlapping segments of dykelets at the upper part of the Lisan section. The Lisan laminae in the overlapping region are displaced. (d) Planar clastic dyke, filled with green clay sediment crosses the upper stiff gypsum layer. Dyke high is about 18 m. (e) Physical connection between a clastic dyke and the source layer (marked by black arrows) 18 m below the surface. Source layer thickness is ∼0.4 m.

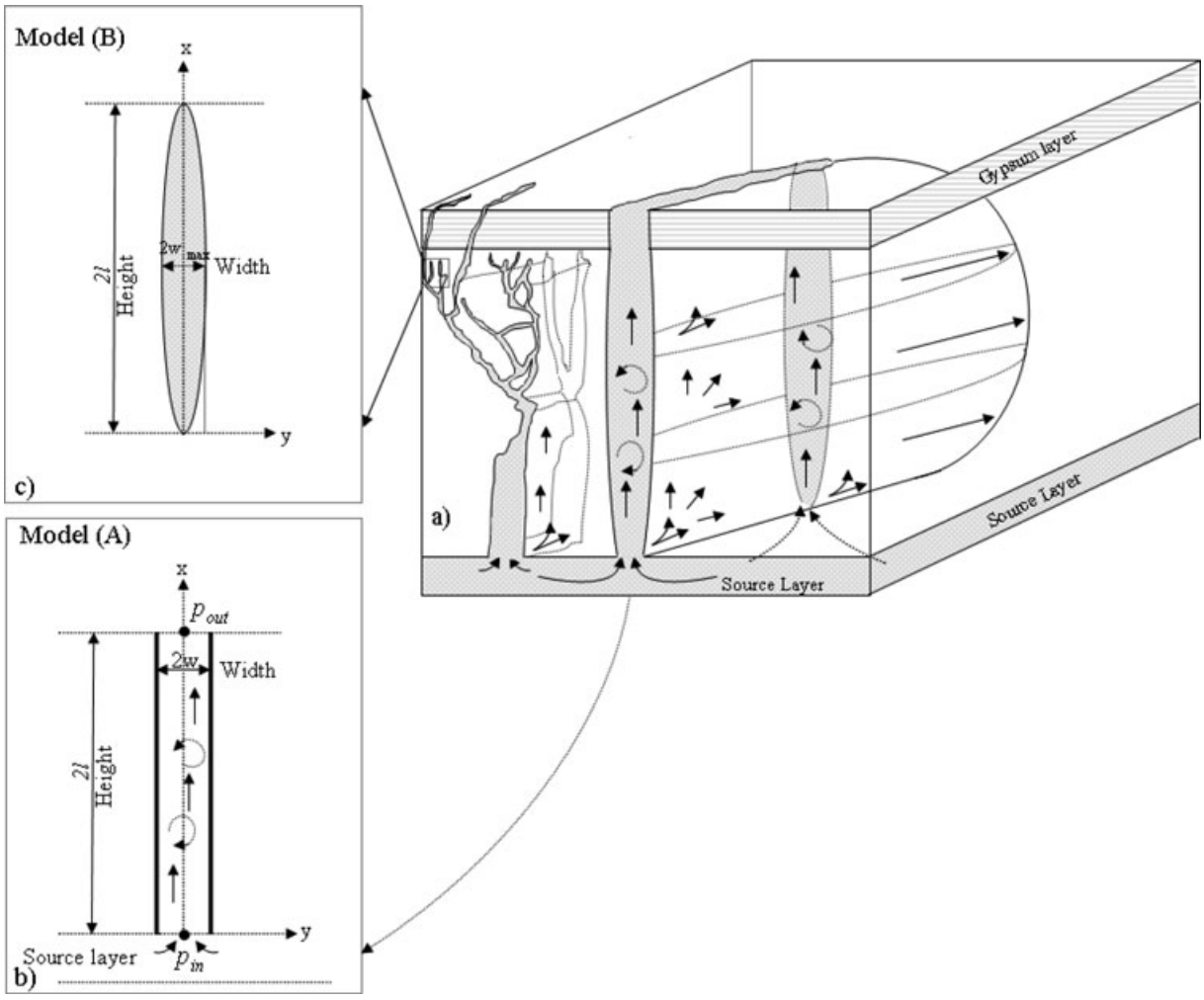

Figure 3. (a) Schematic representation of the two types of dykes: a blade-like dyke with a cross section resembling a channel and a branching dyke and its associated dykelets (left-hand panel). Some dykes/dykelets cross the upper stiff gypsum layer and some do not. (b) Model (A), showing upward flow along the *x*-axis under turbulent flow conditions. (c) Model (B), showing dilation profile of a representative dykelet.

Formation. Part of the upward propagating dykes commonly fracture and open the stiff gypsum layer (Fig. 3a), however, part occasionally terminate against this layer. Several injection dykes, whose width vary between ∼0.1 and 0.18 m, branch upward and split into 3–5 large strands (Fig. 3a). Their pattern resembles the pattern of dynamic fractures that bifurcate during upward propagation (e.g. Bahat *et al*. 2005). The large strands are typically segmented, forming numerous dykelets ∼13 m above the source layer. Assuming that the flow of clastic material followed the fracture propagation implies that the velocity of the fluid during dynamic fracturing could attain high values. The injection velocity could be even higher when the dykes reached the surface because at this stage, the pressure within the source layer is converted only to material flow. Overlapping geometry between two adjacent segments implies opening of a fracture under internal pressure (Fig. 2c; e.g. Delaney & Pollard 1981; Gudmundsson 1995; Weinberger *et al*. 1995).

3 MECHANICAL MODELLING OF THE INJECTION DYKES

3.1 Models for dyke emplacement

We present here two mechanical models that provide some estimate for the source layer pressure and injection velocity of clay-water mixture into the clastic dykes during their emplacement. These models are based on (1) channel flow analysis of planar dykes and (2) elastic crack theory analysis of dyke dilation profiles and the driving pressure distribution in equilibrium state, which are achieved in the last stage of the dyke propagation. The latter analysis is similar to that of magmatic dyke dilation profiles (e.g. Pollard & Muller 1976; Delaney & Pollard 1981; Pollard 1987; Hoek 1994, 1995).

The assumptions for the models of dyke evolution and their justification are based on our interpretation of field observations and AMS analysis (Levi *et al*. 2006a,b). The emplacement process of the dykes may be divided into three consequent stages:

(1) The pressure in the source layer increases to a level that is high enough for nucleation and growth of fractures. However, the details of the nucleation stage and the fluidization process of the source layer are beyond the scope of the present study.

(2) Pressure-driven fractures (i.e. hydro-fractures) start to propagate upwards, downwards and laterally ahead of the injected clay–water mixture that consequently fills the fractures.

(3) The growth of fractures/dykes is mainly upward and laterally because in many cases, they could not cross the stiff gypsum layers that form mechanical boundaries below the source layer. In some cases, the fractures/dykes grew downwards and laterally,

simultaneously with the injection of the clay-water mixture, until they were arrested and the process terminated (Fig. 3a). Levi *et al*. (2006a) demonstrate that expulsion of pore water after the emplacement of the dyke material was minor. Therefore, we assume that the present dyke dimensions should be similar to their dimensions just before the dykes were arrested. The final shape of the dykes may clearly be seen in the dykelets that were emplaced close to the surface, and represent the termination of the dynamic fracturing process (Figs 2b and 3a). Exposing these dykelets in 3-D, by gradual carving and removing the soft Lisan host rock, reveals a decrease (down to disappearance) in their dimensions in all directions. This indicates that the propagation velocity of these dykelets decreased significantly and their growth can be approximated by quasi-static conditions. Hence, a linear elastic analysis of the dykelet dilation profiles provides a first-order approximation of their internal pressure (Fig. 3c). As to the large-scale dykes that propagated up to the surface, channel flow conditions may have occurred at the time before the flow of material ceased.

3.2 Model (A): channel flow

3.2.1 Assumptions and justifications

Levi *et al*. (2006b) analysed the magnetic fabric of the clastic dykes and demonstrated that the AMS signals that evolved resulted from fast flow conditions ($>$cm s^{-1}). The AMS analysis also revealed that although the flow direction was mainly upward, small eddies were generated along the dykes width. This implies that at the final stage of dyke emplacement the clay–water mixture filled the entire dyke width and the flow was fully turbulent.

In this section, we try to constrain the lower cut-off for the pressure gradient needed to assure a turbulent flow in a channel with a designated width, using scaling relations for one-dimensional turbulent flow in a channel with a constant width. The present study deals with fluid flow just before the injection ceased, implying that the channel flow process took place during a short time interval. We also assume that a mean steady-state flow was achieved.

3.2.2 Application to the clastic dykes

We apply scaling relations for 1-D turbulent channel flow (e.g. Turcotte & Schubert 1982). The model assumes an upward flow in the positive x-direction, which is driven by pressure gradient $\frac{\mathrm{d}p}{\mathrm{d}x}$ resulting from two components, the difference between the source layer pressure, p_{in} at $x = 0$ and the pressure at the surface p_{out} at x $= 2l$, and the buoyancy pressure gradient (Fig. 3b). Hence,

$$\frac{\mathrm{d}p}{\mathrm{d}x} = \frac{(p_{\mathrm{out}} - p_{\mathrm{in}})}{2l} + (\rho_{\mathrm{f}} - \rho_r)\, g, \tag{1}$$

where $2l$ is the dyke height, ρ_{r} is the host rock density, ρ_{f} is the fluid density, g is the constant of gravitational acceleration, and p_{in} is the pressure at the source layer.

For turbulent channel flow the pressure gradient is (Prandtl 1942)

$$\frac{\mathrm{d}p}{\mathrm{d}x} = -f\frac{\rho_{\mathrm{f}}\bar{u}^2}{2w}, \tag{2}$$

where $2w$ is the width of the channel (dyke), $\bar{u}$ is the mean velocity and f is the friction factor.

The minus in eq. (2) stands for converting the negative sign of the pressure gradient to a positive value of the viscous resistance and is related to the chosen coordinate system (Fig. 3b).

The friction factor is calculated as follows (Prandtl 1942)

$$f = \frac{0.0791}{\mathrm{Re}^{0.25}}, \tag{3}$$

where $\mathrm{Re} = 2w\bar{u}/\nu$ is the Reynolds number and ν is the kinematic viscosity. For a given Reynolds number the mean velocity in the channel is

$$\bar{u} = \frac{Re\nu}{2w} \tag{4}$$

Combing eqs (1)–(4) enables expressing the pressure at the source layer:

$$p_{\mathrm{in}} = \frac{0.0791\mathrm{Re}^{1.75}\nu^2\rho_{\mathrm{f}}l}{4w^3} + 2(\rho_{\mathrm{f}} - \rho_E)gl + p_{\mathrm{out}}. \tag{5}$$

The Reynolds number controls the transition from the laminar to the turbulent flow. The onset of the turbulent flow in the channel occurs at Re $\approx$ 2200 (e.g. Turcotte & Schubert 1982; Donald 1995). Substituting Re $\approx$ 2200 into eq. (4) and into eq. (5) enables the estimation of a velocity lower limit for the laminar–turbulent transition and thus minimal pressure at the source layer.

p_{out} depends on the conditions in the upper part of the dyke and is equal to the atmospheric pressure 0.1 MPa, if the dyke cuts the upper gypsum layer (Fig. 3a, Geologic Setting) and is open to the surface. This value is associated with the lowermost limit of the pressure in the source layer. The lowermost limit of this pressure, corresponding to the onset of turbulence, increases proportionally to the clay-water mixture viscosity ($\sim\nu^2$) and decreases proportionally to the channel width ($\sim w^{-3}$). This is because the derived formulation assumes that the source layer serves as an infinite reservoir with constant pressure and supplies mass flux into the channel according to its width and clay-water mixture viscosity.

During the dyke growth, the injection velocity could rise up to high values on the order of the fracture velocity. Notably, when fractures made it up to the surface, the injection velocity could be even higher than the fracture velocity (e.g. similar to super-sonic velocities in volcano conduits e.g. Wilson *et al.* 1980). A high value of the pressure in the source layer is estimated, based on high values of the mean velocity u_{upper}. Because emplacement of several dykes is associated with dynamic fracturing (Levi *et al*. 2006a,b) it is likely that the velocity of the low-viscosity clay-water mixture could attain the dynamic velocity of the dyke's leading fracture u_{dynamic}. The dynamic velocity is about half of the Rayleigh wave velocity u_R, which is slightly below the shear wave velocity u_S(e.g. Freund 1998):

$$u_S = \left(\frac{\mu}{\rho_{\mathrm{r}}}\right)^{1/2};\ u_R \approx 0.92u_s \tag{6}$$

where μ is the shear modulus. Hence high value of the velocity is:

$$u_{\mathrm{upper}} \leq u_{\mathrm{dynamic}} \approx 0.5\left(\frac{\mu}{\rho_{\mathrm{r}}}\right)^{1/2} \tag{7}$$

This flow velocity is converted back to a high value for Re using eq. (4) and then to the source layer pressure P_{in} using eq. (5). Note that the high value of the flow velocity is only a comparable value to the fracture dynamic velocity, and it is by no means an upper limit value or physically constrained parameter.

3.3 Model (B): crack elastic analysis of dyke dilation profiles

3.3.1 Assumptions and justifications

The clastic dykes are filled fractures with smooth wall planes that cross-cut the Lisan sediments in a brittle manner. Direct indications

for brittle deformation during dyke emplacement include small-scale faulting and tilting of Lisan lamellae within an overlapping zone between two dyke segments (Fig. 2c). On the other hand, there are no geometrical indications for ductile deformation and viscous fingering between the injected slurry and the Lisan host rock. OSL ages of dyke emplacement suggest that many dykes intruded the Lisan host rock after a significant drop in the Lisan water level (Porat *et al*. 2007). Hence, it is likely that the Lisan sediments lost a significant amount of moisture during these thousands of years, and their properties were similar to those at present. Ductile deformation of the Lisan sediments prior to dyke emplacement is evidenced by tight synsedimentary folds in this formation. Therefore, we assume that brittle fracturing was dominant during dyke emplacement, and hence, elastic theory can be applied to analyse their dilation profiles.

In this model, we assume that the opening profiles of the dykelets are related to the existing pressure gradient, just before the injection process ceased. The pressure gradient is related to the difference between the fluid pressure and the ambient stress in the host rock. The pressure gradient is comparable to the fluid pressure in the associated dykelet because the lithostatic pressure in the upper section of the Lisan host rock is negligible. In addition, because the dykelets were formed in the upper section and were physically connected to the source layer via the large-scale dykes, their pressure gradients can estimate the pressure in the source layer.

3.3.2 Application to the clastic dykes

This section presents the analysis of the measured dilation profiles $2w(x)$ and estimated driving pressure distributions $\Delta p(x)$ for the clastic dykes. Following previous studies (Pollard 1976; Pollard & Muller 1976; Delaney & Pollard 1981; Hoek 1995), driving pressure distributions are approximated by a sum of three linear normal-stress gradients that act on the fracture walls:

$$\Delta p(x) = \Delta p_0 + (\nabla p_a + \nabla p_s)(x - l) \quad \text{for } (0 = x = l), \tag{8a}$$

$$\Delta p(x) = \Delta p_0 + (\nabla p_a - \nabla p_s)(x - l) \quad \text{for } (l < x = 2l) \tag{8b}$$

where l is the half dyke height, x goes from 0 to $2l$ (Fig. 3c), Δp_0 is the uniform normal stress, ∇p_a is the asymmetric linear stress gradient and ∇p_s is the symmetric linear stress gradient. The general dilation profile solution is (Delaney & Pollard 1981):

$$2w(x) = \frac{\Delta p_0}{M}\left[2\sqrt{2xl - x^2}\right] + \frac{\nabla p_a}{M}\left[(x - l)\sqrt{2xl - x^2}\right] + \frac{\nabla p_s}{M}\frac{2}{\pi}\left[l\sqrt{2xl - x^2} + (l - x)^2 \ln\left|\frac{(l - x)}{l - \sqrt{2xl - x^2}}\right|\right], \tag{9}$$

where M is expressed through the shear modulus μ and Poisson's ratio ν_{elastic}:

$$M = \frac{\mu}{(1 - \nu)}. \tag{10}$$

The dilation profile of the dyke is composed of three parts (eq. 9, from left- to right-hand side): (1) the elliptical shape; (2) the teardrop shape and (3) the diamond-shape. The combination of the three dilation profiles results in four models of driving pressure distribution that are analysed by the best-fit method (least squares):

(I) $\Delta p_0 \neq 0, \nabla p_a = 0, \nabla p_s = 0$;
(II) $\Delta p_0 \neq 0, \nabla p_a \neq 0, \nabla p_s = 0$;
(III) $\Delta p_0 \neq 0, \nabla p_a = 0, \nabla p_s \neq 0$;
(IV) $\Delta p_0 \neq 0, \nabla p_a \neq 0, \nabla p_s \neq 0$.

4 ROCK AND FLUID PROPERTIES

The mechanical properties of the Lisan sediments were seldom measured due to their weakness and fragility. Hence, we use published data on soft sediments including that obtained on the late Pleistocene lacustrine Samra Formation (Chetrit 2004), which sedimentologically is similar to the Lisan Formation. Soft sediments possess higher Poisson's ratios than hard rocks (Othman 2005). Therefore, we used 0.4 for the Poisson's ratio, which is also in agreement with the suggested 0.3–0.5 values of clay-rich sediments (e.g. Gee-Clough *et al*. 1994; Vallejo & Lobo-Guerrero 2002; Chetrit 2004; Othman 2005; Bala *et al*. 2006). For the dykelets developed close to the surface, we used a range of shear modulii between 50 to 100 MPa (e.g. Bala *et al*. 2006). For the entire Lisan section, we set a shear modulus equal to 100 MPa, which is in agreement with other experiments of soft sediments (e.g. Gannon *et al.* 1999; Schneider *et al*. 1999; Chetrit 2004; Yuan-qiang & Xu 2004; Bala *et al.* 2006). The rock density for the whole Lisan section was set to 1400 kg m^{-3}, and the maximum tensile strength is about $T_o = 0.1$ MPa (Arkin & Michaeli 1986). These values were applied to the analyses of dyke dilation profiles. There is no direct information about the water quantity during the injection process. Reasonable viscosity values can be suggested based on the geologic setting of the dykes and viscosity experimental tests carried out in the present study. For the channel flow analysis we used two values of kinematic viscosity, $\nu = 0.3\text{E}-04$ m^2 s^{-1} and $1.5\text{E}-04$ m^2 s^{-1} (Appendix), where the Lisan clay-water mixture density is 1700 kg m^{-3} and 1950 kg m^{-3}, respectively.

5 RESULTS

5.1 Model (A)

The model starts by calculating the maximum injection velocity using eq. (4). Eighteen runs were preformed for nine channel widths (0.05, 0.07, 0.09, 0.1, 0.12, 0.14, 0.16, 0.18 and 0.2 m) and two kinematic viscosities (0.3E−04 and 1.5E−04 m s^{-1}). The upper Re was set for each dyke width according to the upper velocity calculated by eq. (7).

The calculated injection velocities vary from 0.2 to $\sim$ 250 m s^{-1} and the corresponding values of Re vary between 2.2×10^3 and $\sim 1 \times 10^6$ (Fig. 4). The lowest value of the injection velocity was obtained for a kinematic viscosity of 0.3E − 04 m^2 s^{-1}, dyke width of 0.2 m and Re $= 2.2 \times 10^3$ (Fig. 4, run i1). Higher values were obtained in every run by increasing the Reynolds number (Fig. 4). Based on the upper Re values obtained for each run in Fig. 4 ($42 \times 10^3 \leq \text{Re} \leq 90 \times 10^4$), the pressure at the source layer calculated by eq. (5) varies between $\sim$0.2 and $\sim$65 MPa. The lowest and highest pressure values obtained are for run i1 and run a2, respectively (Fig. 5).

Variations in the dyke widths (thicknesses) resulted in significant velocity changes of tens of metres per second and pressure changes of several MPa (e.g. run d2 and run a2 in Figs. 4 and 5). Variations of the dynamic viscosity also resulted in significant velocity changes on the order of tens of metres per second and pressure changes of several MPa (e.g. run a1 and run a2 in Figs. 4 and 5).

5.2 Model (B)

The geometric analysis of five dykelets is presented in Figs 6(a) and (b). The driving pressure distributions are calculated by analyzing the coefficients of eq. (9) and using eqs 8(a) and (b) (Figs 7a and b).

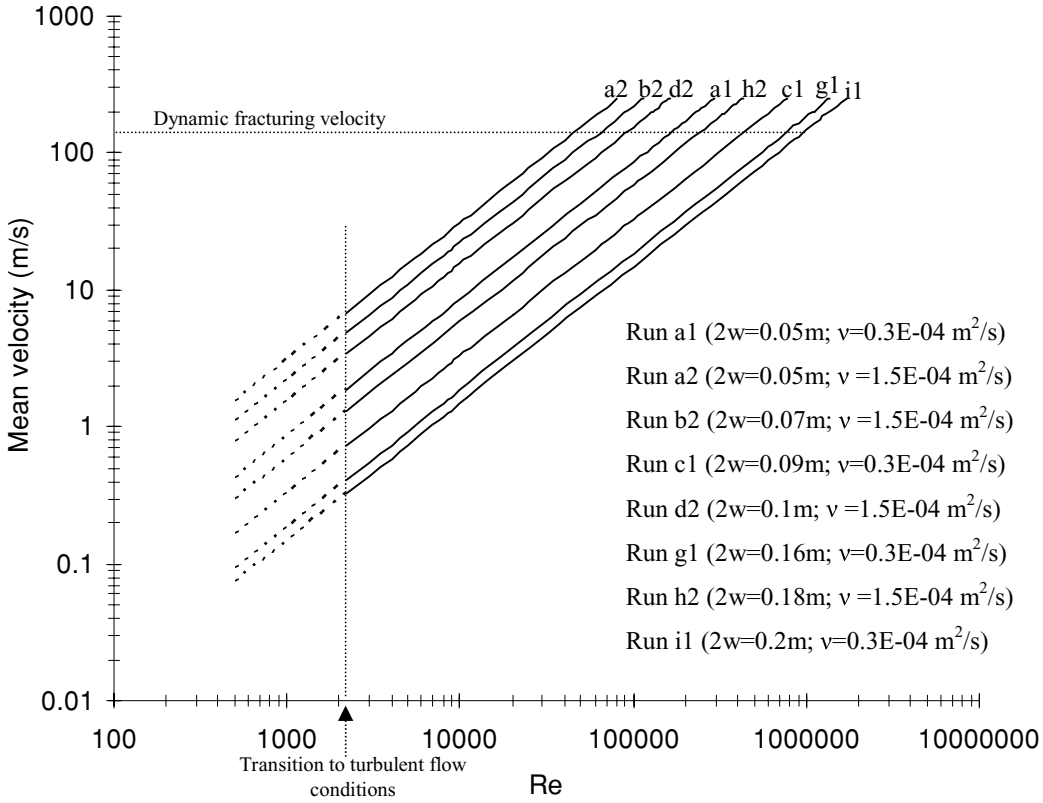

Figure 4. Results of model B, showing the mean injection velocity as a function of Re plotted on log-log graph (eq. (4)). The vertical dashed line marks the transition between laminar flow and turbulent flow at Re = 2200, and therefore the lower possible velocity limit for turbulent flow of the clastic material. High velocity values, comparable to the dynamic fracture velocity as calculated by eq. (7), are marked by the horizontal dashed line. Pairs of width, $2w$, and the kinematic viscosity, ν, for each run are denoted in parentheses.

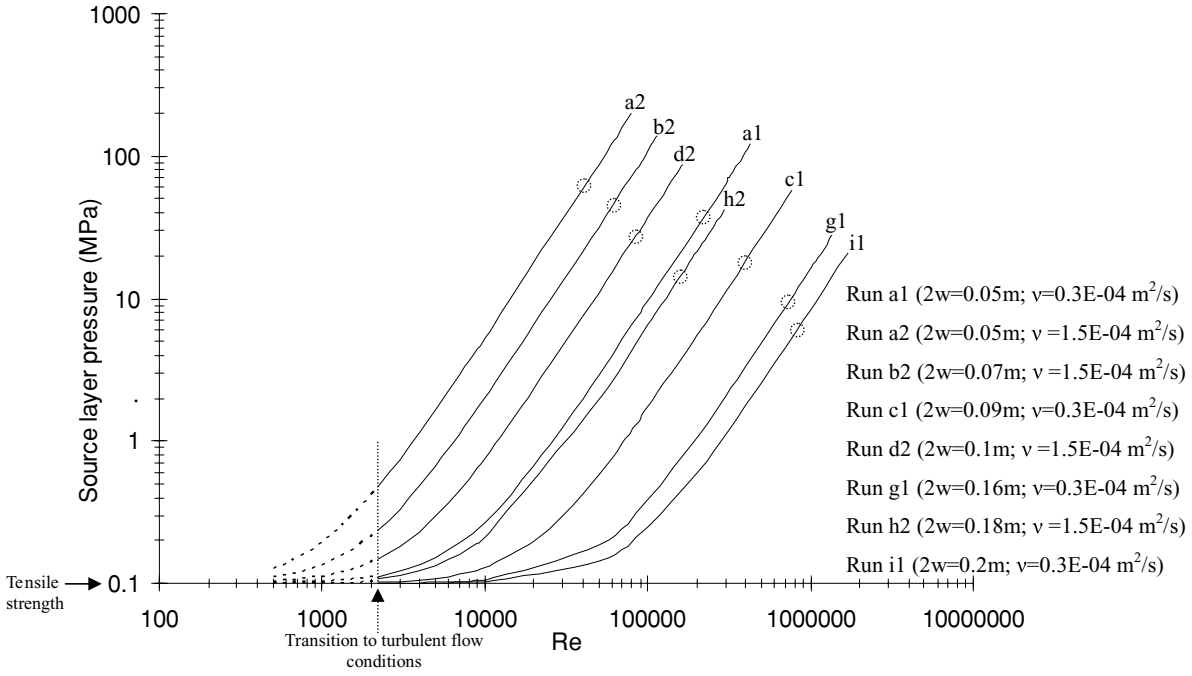

Figure 5. Results of model (A), showing pressure at the source layer as a function of Re plotted on log–log graph (eq. 5). The runs calculated by eq. (4) stop arbitrarily at Reynolds numbers that are related to $\sim$250 m s^{-1}. The dashed circles denote the possible upper pressures calculated by using the Reynolds numbers that are related to the high velocity values in Fig. 4. The pressure lower limit in the curves is related to Re = 2200 and marked by the dashed line and the tensile strength $T_o \approx 0.1$ MPa. Note that pressures of the order of the tensile strength (<0.5 MPa) are not realistic, because the flow occurs under turbulent flow conditions.

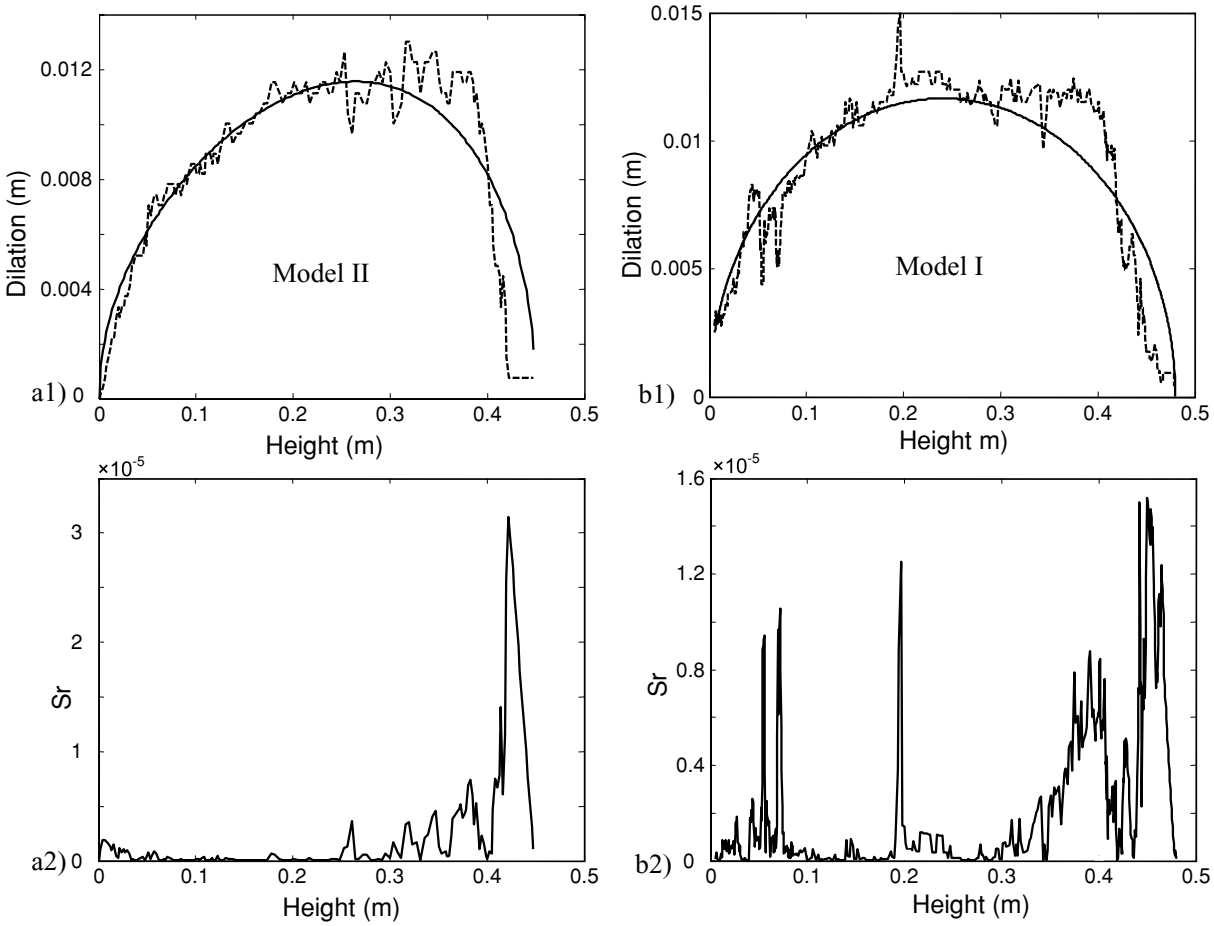

Figure 6. Results of model (B), showing the measured (dashed line) and the modeled (solid line) dilation profile (eq. 9) of two representative clastic dykes (a1, b1; fracture 1 and fracture 2 in Table 1) and their sum of errors (a2, b2). The appropriate model is marked on the profile.

High R^2 values for the four models I–IV imply that the elastic openings of the dykelets fit well with the linear elastic theory. Model II and model IV generally have higher r-squared values (Table 1). The average driving pressures for both $G = 50$ and 100 MPa calculated by model IV is ∼4 MPa (Fig. 7).

6 DISCUSSION

During strong earthquakes, tensile stresses are induced at the surface, forming tensile fractures at the Earth's surface (e.g. Dalguer *et al*. 2002). Such fissures could be passively filled with clastic sediment from above (e.g. Eyal 1988), forming so-called Neptunian dykes. Field observations strengthened by magnetic AMS flow analysis demonstrated that the clastic dykes presented in the Ami'az Plain, Lisan Formation, Dead Sea basin, were formed due to the injection of clay-water mixture (Levi *et al*. 2006a,b). Therefore, we suggest that the values of the driving pressures discussed below represent the internal pressure in the source layer.

6.1 Driving pressures and injection velocities

The two models presented in this study provide a tool for estimating the injection velocities and driving pressures during the clastic dykes emplacement. To get reliable results, we used a range of rock and fluid properties, which are based on our laboratory measurements of viscosity (Appendix) and on published data of clay-rich sediments. The injection through the dyke-channel (Model A) is considered, based on the measured viscosities, to be Newtonian–Poiseuille flow. This allows us to provide a first order approximation of the dyke flow velocities and pressures during earthquake events. Numerical simulations of non-Newtonian flow within the dykes are beyond the scope of the present study and will be presented in a follow-up paper.

The estimation of the lower limit for the driving pressure and injection velocity is based on scaling relations for 1-D turbulent flow in a channel with a constant width. This approach (Model A) estimates the minimal driving pressure (Fig. 8) needed to assure a turbulent flow in a channel of a designated width. The lower grey polygon marks the range of minimal driving pressures, calculated by using the lowest value ($\nu = 0.3$E-04 m^2 s^{-1}) and the highest value ($\nu = 1.5$E – 04 m^2 s^{-1}) of the laboratory-measured kinematic viscosity. Fig. 7 demonstrates the distribution of driving pressure calculated with model (B) for every dykelet. Bars shown in Fig. 8 correspond to the maximal and minimal values of these pressure distributions and define the polygon bounding the estimated pressure range based on model (B). The dykelets analysed here resulted from dynamic branching of the relatively wide dykes (0.1–0.18 m). Hence, the obtained pressure range of model (B) could be viewed as a lower limit for the driving pressure for this group of dykes. The most probable range of driving pressures for wide dykes falls within 1–25 MPa, where the lower limit of the pressure

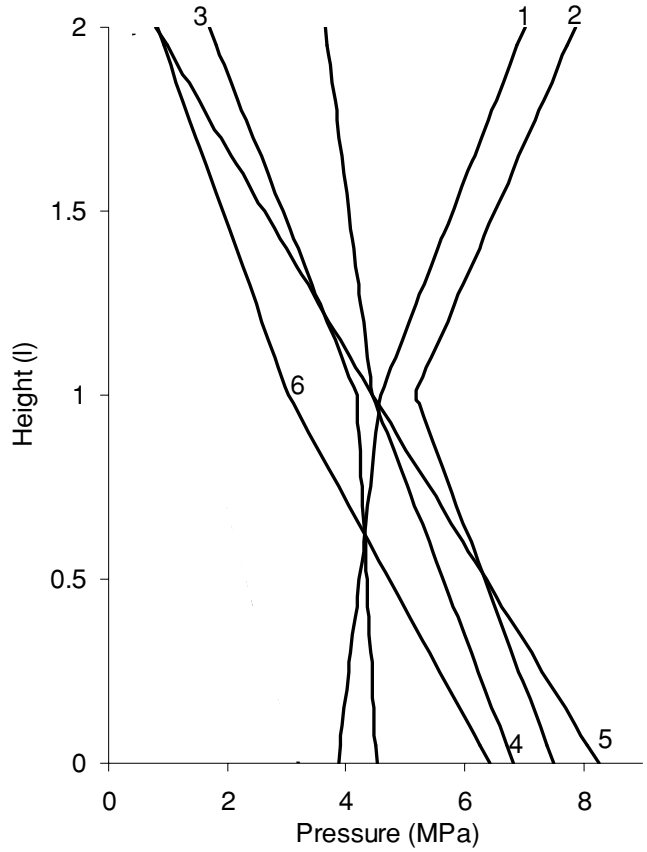

Figure 7. Pressure distribution (eqs 8a and b) marked by solid line along representative dykelets using model IV and G = 100 MPa. Numbers are related to fracture number in Table 1. The range of the pressure values are limited by fracture 2 and fracture 6.

Table 1. Output of Model B.

Number	Fracture type	R^2 per mode type			
		I	II	III	IV
1	Fracture 1-single fracture	0.87	0.90	0.88	0.90
2	Fracture 2-single fracture	0.99	0.99	1.00	1.00
3	Fracture 3-single fracture	0.91	0.94	0.91	0.94
4	Fracture 4-segment a	0.85	0.90	0.86	0.91
5	Fracture 4-segment b	0.81	0.95	0.81	0.95
6	Fracture 4-segment a & segment b	0.74	0.93	0.74	0.93

is based on model (B) and the high value on model (A). Finally, the overlapping driving pressures of the two models are between 1 and 10 MPa (Polygon #1, Fig. 8). Because the two different models give an overlapping range of driving pressures, it is most probably that this range of driving pressures existed within the source layer. It is most likely that wider dykes, associated with large elastic deformations, were emplaced under higher driving pressures, probably generated by stronger seismic events or due to more efficient local pressure build-up in the source layer. We note that the higher values of driving pressures in polygon #1 fall very close to the driving pressures obtained for dynamic fracture velocity (Fig. 8, upper grey strip), and therefore, dynamic branching of the wider dykes is very reasonable.

Scaling relations for 1-D turbulent flow in a channel also enables to estimate the injection velocities. Based on the lower value of the driving pressure (1 MPa), we derived the associated Re numbers from Fig. 5 and, consequently, substituted them in Fig. 4 to obtain a lower value for the injection velocity of ∼10 m/s. For a range of injection velocities between 10 and 130 m s^{-1} (i.e. dynamic fracture velocity), the duration of dyke emplacement is ∼0.1–2 s for a 18-m-high dyke.

Branching or small dykelets connected to the main channel were never observed in association with relatively narrow dykes (<0.1 m). Therefore, we speculate that the narrow dykes were emplaced under driving pressures equal (polygon #2a) or lower (polygon #2b) than the pressures of the polygon #1. Even if the narrow dykes were emplaced during the same seismic event and were driven by the same pressure, their injection velocity is expected to be lower than that of the wide dykes and fall below the threshold of dynamic branching. These dykes could also be formed due to a lower driving pressures, marked by the polygon #2b. Still, the injection velocity of the narrow dykes is estimated to be 1 m s^{-1} corresponding to the duration of the dyke emplacement 18 s.

The above velocities are comparable to velocities obtained during a hydro-abrasive erosion process in brittle materials in which material is removed by high speed of water jet mixed with solid particles. The velocity of a water jet that succeeded in penetrating soft rocks varied from 92 to 200 m s^{-1} and was associated with pressure between 5 and 22 MPa (Momber 2004). The predicted velocity for sand liquefaction is about 2 m s^{-1} (Gallo & Woods 2004), which is within the lower range of velocities that were obtained in the present study for clastics injected into dykes.

For flow of sand-water mixtures in 10–100 m height vertical conduits, Gallo & Woods (2004) calculated overpressures between 0.35 to 1 MPa. In their model, the overpressures are formed due to the difference between the densities of the host rock and the sand-water mixture. Pressure gradients results from the difference between the overpressures and the frictional resistance, similar to the evolved pressure gradients in the present model (see eq. 5). The models of this study calculate the velocities needed to obtain a turbulent flow, and based on these velocities, determine the pressures that are also consistent with that needed to dilate the fractures. The obtained pressures for the present geological setting and mechanical approach are about one order of magnitude higher than those of Gallo & Woods (2004).

Jolly & Lonergan (2002) calculated an overpressure of several MPa for a sandy source layer at hundreds of metres below the surface. In their model, similar to that of Gallo & Woods (2004), the overpressure is built-up by the difference between the host rock and the sand-water mixture densities. However, the injection velocities, as well as the dyke dilation, were not considered. Their calculations cannot be directly applied to clastic dykes at shallow depth, such as those in the Lisan Formation, because the differences between the Lisan host rock and the clay-water mixture densities are insufficient to drive a turbulent flow. The pressure-driven mechanism of the clastic dykes emplacement is compatible with field observations, demonstrating that in the same injection system the flow can be upward, horizontal and even downward (Levi *et al*. 2006b).

6.2 Pressures during earthquakes

The response of materials to a sudden applied stress is still not well understood (e.g. Sawicki & Mierczynski 2006), especially for clay-rich sediments (Yılmaz *et al*. 2004). So far, only a few studies have dealt with the fluidization mechanism of soft sediments during earthquake loading. Most of them suggest that the direct impact of the *p*-wave loading that passed through the

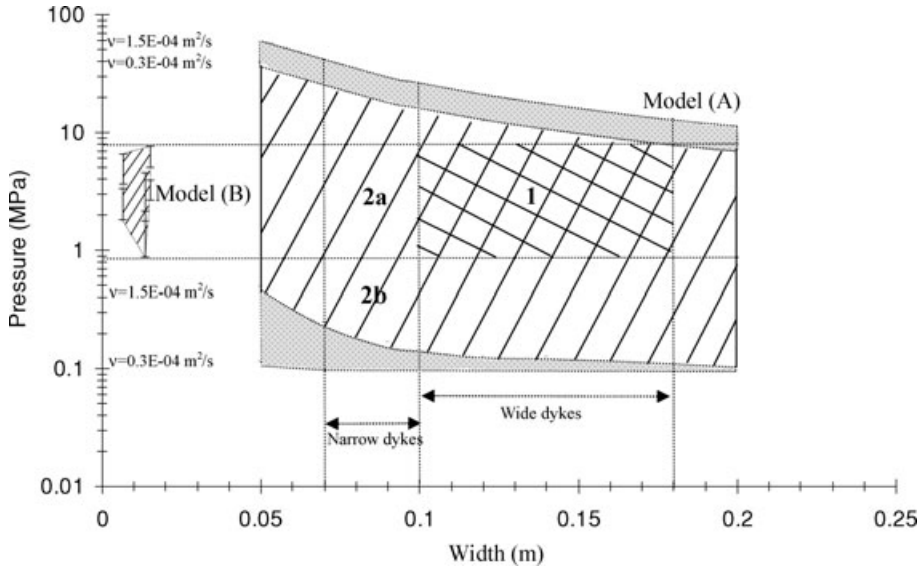

Figure 8. Range of possible pressures in the source layer versus the width of the clastic dykes calculated by using model (A) and model (B). The grey polygons mark the minimal and maximal pressures calculated using model (A) with kinematic viscosity $\nu = 0.3\text{E}-04\ \text{m}^2\ \text{s}^{-1}$ and $\nu = 1.5\text{E}-04\ \text{m}^2\ \text{s}^{-1}$. Bars correspond to the pressure range for each dykelet calculated using model (B) and presented in Fig. 7. The polygon bounding these bars defines the estimated pressure range based on model (B). Polygons #1 and #2 represent the most probable range of driving pressures for wide and narrow dykes estimated by integrating models (A) and (B).

poro-elastic medium causes fluidization (e.g. Melosh 1996; Sornette & Sornette 2000; Bachrach *et al.* 2001; Collins *et al.* 2002). By seismic wave, loading the soft sediments are dynamically fluidized without the need of a lithostatic-compaction effect (Bachrach *et al*. 2001). In acoustic fluidization (e.g. Collins *et al.* 2002), the transient *p* waves and pressure fluctuations within the source layer may temporarily relieve the overburden pressure and, hence, abrogate the internal frictional strength of the medium. The theory, therefore, predicts a rheology where stresses are supported without appreciable strain, unless acoustic vibrations in the medium are strong enough to reduce the material resistance to shear and flow occurs.

The present study does not allow a definite conclusion whether fluidization during an earthquakes in the Dead Sea basin was promoted by dynamic or static stresses. Yet, it is more likely that fluidization resulted from dynamic stresses, because static pressure alone could not provide the trigger for fluidization of the Lisan clay-rich sediments, especially because the water content involved in the fluidization could be relatively low (Levi *et al.* 2006b). The Lisan host rock consists mainly of the authigenic chalk ('the ambient rock') and wet clay layers. Shaking and squeezing of the clay-rich sediments causes a fast expulsion of pore water, a drastic loss of shear strength and consequent material flow within host rock. This shaking could not fluidize the authigenic chalk of the Lisan, because its textural and mechanical properties are not in favour for losing shear strength in such conditions. Furthermore, resetting of quartz OSL signals that occurred during the emplacement of the clastic dykes in the Ami'az Plain, were reported (Porat *et al*. 2007). It is suggested that the resetting occurred due to pressure build-up within the dykes during the injection process. Eddingsaas & Suslick (2006) suggested a mechanism in which shock waves that accelerate micrometre-sized particles to high velocities result in interparticle collisions in the liquid and create a mechanoluminescence effect. This effect, caused by shock waves, may explain the resetting effect of the OSL and provide additional support for the interaction between the clay-rich sediment and the seismic waves induced during earthquakes. Therefore, it is most likely that the fluidization process that formed within the source layer is directly related to the impact of the acoustic waves, as suggested by Collins *et al.* (2002). Hence the obtained parameters should be discussed in the context of the fluidization related to the dynamic stresses generated during earthquake events.

Kanamori & Anderson (1975) analysed the moment–area scaling for interplate earthquakes with surface magnitude $M_S > 5.8$ and suggested a range of the static stress drop between 1 and 10 MPa. This range was confirmed by analysis of source parameters of strong historical earthquakes (Wells & Coppersmith 1994). The dynamic stress drop, calculated for several strong earthquakes close to the earthquake source zone, has similar values or slightly above the values of the static stress drop. Ichinose *et al.* (1997) calculated the dynamic stress drop for the Basin and Range earthquakes and got values between 1 and 10 MPa. In the area surrounding the nucleation zone of the 2000 Tottori (Japan) earthquake, Dalguer *et al.* (2002) calculated a dynamic stress drop between 5 and 30 MPa. Iwata *et al.* (2004) calculated, for strong motion earthquakes, a dynamic stress drop between 5 and 20 MPa. From near-fault seismic data of the 1999 Chi-Chi (Taiwan) earthquake, Huang *et al.* (2001) reported a dynamic stress drop of 6.5 MPa for the southern segment and 30 MPa for the northern one. For the same earthquake, Hwang *et al.* (2001) reported a dynamic stress drop of 11.2 MPa for the southern segment and 20 MPa for the northern one. At this stage, we can attest to the similarities between the stress (pressure) values (1–10 MPa) calculated for the injected clastic dykes and the dynamic stress drop values associated with strong earthquakes.

7 CONCLUSIONS

(1) The emplacement time of the clastic dykes in the Ami'az Plain ranges between 0.1 and 18 s, and the injection velocity could reach tens of metres per second. Hence, the injection of clastic dykes during earthquakes manifests dynamic processes that were associated with these events.

(2) The pressure at the Lisan source layer could reach several to tens of MPa. This high pressure is probably an expression of the seismic waves that passed through the source layer in the proximity to the earthquake source region.

(3) The pressure required to fluidize the Lisan clay-rich sediment at the source layer might be higher than the pressure needed to dilate the associated clastic dykes.

(4) Injection of clastic dykes may serve as evidence for seismic processes that occur close to active faults. Their geometrical and kinematical analyses pose constraints on the pressure values associated with strong palaeo-earthquakes, which can hardly be estimated otherwise.

ACKNOWLEDGMENTS

This study was supported by a grant from the Israeli Ministry of National Infrastructures. We are indebted to Yehuda Ben-Zion and two anonymous reviewers for providing constructive and helpful reviews. TL thanks Avihu Levi for helping to reconstruct the algorithm in model (B) and Moshe Arnon and Yaacov Rafael for their help in the field.

We are greatful to Daniela Hershkovitz and Nava Devon for their invaluable help in conducting the viscosity experiments.

REFERENCES

Arkin, Y. & Michaeli, L., 1986. The significance of shear strength in the deformation of laminated sediments in the Dead Sea area, *Isr. J. Earth Sci.,* **35,** 61–72.

Bachrach, R., Nur, A. & Agnon, A., 2001. Liquefaction and dynamic poroelasticity in soft sediments, *J. geophys. Res.,* **106**(B7), 13515–13526.

Bahat, D., Rabinovitch, A. & Frid, V., 2005. *Tensile Fracturing in Rocks*, Springer-Verlag, Berlin, 557 p.

Bala, A., Raileanu, V., Zihan, I., Ciugudean, V. & Grecu, B., 2006. Physical and dynamic properties of the shallow sedimentary rocks in the Bucharest metropolitan area, *Rom. Rep. Phys.*, **58**(2), 221–250.

Begin, Z.B., Louie, J.N., Marco, S. & Ben-Avraham, Z., 2005. *Prehistoric Seismic Basin Effects in the Dead Sea Pull-apart*, The Ministry of National Infrastructures Geological Survey of Israel Report GSI/04/05, 31 p.

Begin, Z.B., Nathan, Y. & Ehrlich, A., 1980. Stratigraphy and facies distribution in the Lisan Formation—new evidence from the area south of the Dead Sea, Israel, *Isr. J. Earth Sci.,* **29,** 182–189.

Ben-Menahem, A., Nur, A. & Vered, M., 1976. Tectonics, seismicity and structure of the Afro-Eurasian junction—the breaking of an incoherent plate, *Phys. Earth planet. Inter.,* **12,** 1–50.

Chetrit, M., 2004. Subsurface structure at the NW coast of the Dead Sea—a geophysical study (in Hebrew, English abstract). *M.Sc. thesis*. Ben-Gurion University of the Negev, 66 p.

Collins, G.S., Melosh, H.J., Morgan, J.V. & Warner, M.R., 2002. Hydrocode simulations of chicxulub crater collapse and peak-ring formation, *Icarus*, **157,** 24–33.

Dalguer, L.A., Irikura, K. & Zhang, W., 2002. Distribution of dynamic and static stress changes during 2000 Tottori (Japan) earthquake: brief interpretation of the earthquake sequences; foreshocks, mainshock and aftershocks, *Geophys. Res. Lett.*, **29**(16), 1–4.

Delaney, P.T. & Pollard, D.D., 1981. Deformation of host rocks and flow of magma during growth of Mintette dykes and breccia-bearing intrusions near Ship Rock, New Mexico, *U.S. Geol. Surv. Prof. Paper.*, **1202,** 1–61.

Donald, J.O., 1995. Inner region of smooth pipes and open channels, *J. Hydr. Eng.*, **121,** 555–560.

Eddingsaas, N.C. & Suslick, K.S., 2006. Light from sonication of crystal slurries, *Nature,* **444,** 163.

Enzel, Y., Kadan, G. & Eyal, Y., 2000. Holocene earthquakes inferred from a fan-delta sequence in the Dead Sea graben, *Quatern. Res.,* **53,** 34–48.

Eyal, Y., 1988. Sandstone dykes as evidence of localized transtension in a transpressive regime, Bir Zreir area, Eastern Sinai, *Tectonics,* **7,** 1279–1289.

Freund, L.B., 1998. *Dynamic Fracture Mechanics,* Cambridge University Press, Cambridge, 581 p.

Freund, R., Zak, I. & Garfunkel, Z., 1968. Age and rate of sinistral movement along the Dead Sea Rift, *Nature,* **220,** 253–255.

Galli, P., 2000. New empirical relationships between magnitude and distance for liquefaction, *Tectonophysics,* **324,** 169–187.

Gallo, F. & Woods, A.W., 2004. On steady homogeneous sand–water flows in a vertical conduit, *Sedimentology,* **51,** 195–210.

Gannon, J.A., Masterton, G.G.T., Wallace, W.A. & Wood, D.M., 1999. Piled foundations in weak rock, *Sharing Knowledge Building Best Practice,* CIRIA Report, 37 p. (Reprinted in 2004 London).

Garfunkel, Z., 1981. Internal structure of the Dead Sea leaky transform in relation to plate kinematics, *Tectonophysics,* **80,** 81–108.

Gee-Clough, D., Wang, J. & **W(Worsak)** Kanok-Nukulchai, 1994. Deformation and failure in wet clay soil, part 3: finite element analysis of cutting of wet clay by Tines, *J. Agric. Engineer. Res.,* **58,** 121–131.

Gudmundsson, A., 1995. The geometry and growth of dykes. Makhtesh Ramon, Israel, in *Physics and Chemistry of Dykes,* pp. 23–34, eds, Baer, G. & Heimann, A., Balkema, Rotterdam.

Haase-Schramm, A., Goldstein, S.L. & Stein, M., 2004. U-Th dating of Lake Lisan aragonite (late Pleistocene Dead Sea) and implications for glacial East Mediterranean climate change, *Geochim. Cosmochim. Acta,* **68,** 985–1005.

Hoek, J.D., 1994. Mafic dykes of the Vesfold Hills, East Antarctica: an analysis of tholeitic dyke swarms and of the role dyke emplacement during crustal extension, *PhD thesis*. Universiteit Utrecht.

Hoek, J.D., 1995. Dyke propagation and arrest in Proterozoic tholeitic dyke swarms, Vesfold Hills, East Antarctica, in *Physics and Chemistry of Dykes,* pp. 79–93 eds Baer, G. & Heimann, A., Balkema, Rotterdam.

Hofstetter, A., 2003. Seismic observations of the 22/11/1995 Gulf of Aqaba earthquake sequence, *Tectonophysics,* **369,** 21–36.

Huang, W.G., Wang, J.H., Huang, B.S., Chen, K.C., Hwang, R.D., Chang, T.M., Chiu, H.C. & Tsai, C.C., 2001. Estimates of source parameters for the Chi-Chi, Taiwan, earthquake, based on Brune's source model, *Bull. seism. Soc. Am.,* **91,** 1190–1198.

Hwang, R.D., Wang, J.H., Huang, B.S., Chen, K.C., Huang, W.G., Chang, T.M., Chiu, H.C. & Tsai, C.C., 2001a. Estimates of stress drop from near-field seismograms of the Ms7.6 Chi-Chi, Taiwan, earthquake of September 20, 1999, *Bull. seism. Soc. Am.,* **91,** 1158–1166.

Ichinose, G.A., Smith, K.D. & Anderson, J.G., 1997. Source parameters of the 15 November 1995 Border Town, Nevada, earthquake sequence, *Bull. seism. Soc. Am.,* **87,** 652–667.

Iwata, T., Sekiguchi, H., Miyake, H., Zhang, W. & Miyakoshi, K., 2004. Dynamic source parametres and characterized source model for strong motion prediction. *13th World Conference on Earthquake Engineering Vancouver, B.C., Canada August 1–6 (2004),* paper No. 2392.

Jolly, R.J.H. & Lonergan, L., 2002. Mechanisms and controls on formation of sand intrusions, *J. Geol. Soc., Lond*., **159,** 605–617.

Kanamori, H. & Anderson D. L., 1975. Theoretical basis of some empirical relations in seismology, *Bull. seism. Soc. Am.,* **65,** 1073–1095.

Ken-Tor, R., Agnon, A., Enzel, Y., Stein, M., Marco, S. & Negendank, J.F.W., 2001. High-resolution geological record of historic earthquakes in the Dead Sea basin, *J. geophys. Res.,* **106,** 2221–2234.

Levi, T., Weinberger, R., Aïfa, T., Eyal, Y. & Marco, S., 2006a. Earthquake-induced clastic dykes detected by anisotropy of magnetic susceptibility, *Geology,* **34,** 69–72, doi:10.1130/G-22001.1

Levi, T., Weinberger, R., Aïfa, T., Eyal, Y. & Marco, S., 2006b. Injection mechanism of clay-rich sediments into dykes during earthquakes, *Geochem. Geophys. Geosyst.,* **7**(2) 1–20, Q12009, doi:10.1029/2006GC001410.

Marco, S. & Agnon, A., 1995. Prehistoric earthquake deformation near Masada, Dead Sea graben, *Geology,* **23,** 695–698.

Marco, S., Stein, M., Agnon, A. & Ron, H., 1996. Long term earthquake clustering: a 50,000 year paleoseismic record in the Dead Sea graben, *J. Geophys. Res.,* **101,** 6179–6192.

McCalpin, J.P., 1996. *Paleoseismology. International Geophysical Series,* 62nd ed., Academic Press, San Diego, 588 p.

Melosh, H.J., 1996. Dynamical weakening of faults by acoustic fluidization, *Nature,* **379,** 601–606.

Mohindra, R. & Bagati, T.N., 1996. Seismically induced soft-sediment deformation structures (seismites) around Sumdo in the lower Spiti valley (Tethys Himalaya), *Sediment. Geol.,* **101,** 69–83.

Momber, A.W., 2004. Synergetic effects of secondary liquid drop impact and solid particle impact during hydro-abrasive erosion of brittle materials, *Wear,* **256,** 1190–1195.

Moretti, M., 2000. Soft-sediments deformation structures interpreted as seismites in middle-late Pleistocene aeolian deposits (Apulian foreland, southern Italy), *Sediment. Geol.,* **135,** 167–179.

Othman, A.A.A., 2005. Construed geotechnical characteristics of foundation beds by seismic measurements, *J. Geophys. Engineer.,* **2,** 126–138.

Pollard, D.D., 1976. On the form and stability of open fractures in the earth's crust, *Geophys. Res. Lett.,* **3,** 513–516.

Pollard, D.D., 1987. Elementary fracture mechanics applied to the structural interpretation of dykes, in Mafic dyke swarms, *Geol. Assoc. Canada Spec. Paper,* Vol. 34, 5–24. eds Halls, H.C. & Fahrig, W.F.

Pollard, D.D. & Muller, O.H., 1976. The effect of gradients in regional stress and magma pressure on the form of sheet intrusions in cross section, *J. Geophys. Res.,* **81**(5), 975–984.

Porat, N., Levi, T. & Weinberger, R., 2007. Possible resetting of quartz OSL signals during earthquakes—evidence from late Pleistocene injection dykes, Dead Sea basin, Israel, *Quatern. Geochron.,* **2,** 272–277.

Prandtl, L., 1942. *Führer durch die Strömungslehre,* Vieweg und Sohn, 648 pp.

Quennell, A.M., 1959. Tectonics of the Dead Sea Rift, in *Proceedings of the 20th International Geological Congress,* pp. 385–405.

Rodríguez-Pascua, M.A., Calvo, J.P., De Vicente, G. & Gómez-Gras, D., 2000. Soft-sediment deformation structures interpreted as seismites in lacustrine sediments of the Prebetic Zone, SE Spain, and their potential use as indicators of earthquake magnitudes during the Late Miocene, *Sediment. Geol.,* **135,** 117–135.

Sawicki, A. & Mierczynski, J., 2006. Developments in modeling liquefaction of granular soils, caused by cyclic loads, *Appl. Mech. Rev.,* **59,** 91–106.

Schneider, J.A., Hoyos, L., Jr., Mayne, P.W., Macari, E.J. & Rix, G.J., 1999. Field and laboratory measurements of dynamic shear modulus of Piedmont residual soils, *Behavioral characteristics of residual soils*, GSP, Vol. 92, pp. 12–25, ASCE, Reston, VA.

Seed, H.B., 1979. Soil Liquefaction and cyclic mobility for level ground during earthquakes, *J. Geotech. Eng., Am. Soc. Civ. Eng.,* **97,** 1249–1274.

Shapira, A., Avni, R. & Nur, A., 1993. A new estimate for the epicenter of the Jericho earthquake of 11 July 1927, *Isr. J. Earth Sci.,* **42**(2), 93–96.

Sharon, E., Gross, S.P., Fineberg, J., 1996. Energy dissipation in dynamic fracture, *Phys. Rev. Lett*., **76,** 2117–2120.

Sornette, D. & Sornette, A., 2000. Acoustic Fluidization for Earthquakes? *Bull. Seism. Soc. Am.,* **90**(3), 781–785.

Turcotte, D.L. & Schubert, G., 1982. *Geodynamics: Application of Continuum Physics to Geological Problems,* John Wiley, Hoboken, NJ.

Umutlua, N., Koketsub, K. & Milkereit, C., 2004. The rupture process during the 1999 Dqzce, Turkey, earthquake from joint inversion of teleseismic and strong-motion data, *Tectonophysics,* **391,** 315–324.

Vallejo, L.E. & Lobo-Guerrero, S., 2002. The elastic modili of soils with dispersed oversize, in *Proceedings of the 15th ASCE Engineering Mechanics Conference June 2–5, 2002,* Columbia University, New York, NY.

Vardy, A.E. & Brown, J.M.B., 2004. Transient turbulent friction in fully rough pipe flows, *J. Sound Vibr.,* **270,** 233–257.

Weinberger, R., Baer, G., Shamir, G. & Agnon, A., 1995. Deformation bands associated with dyke propagation in porous sandstone. Makhtesh Ramon, Israel. In *Physics and Chemistry of Dykes,* pp. 95–112, eds Baer, G. & Heimann, A., Balkema, Rotterdam.

Weinberger, R., Lyakhovsky, V., Baer, G. & Begin, Z.B., 2006a. Mechanical modeling and InSAR measurements of Mount Sedom uplift, Dead Sea basin: Implications for rock-salt properties and diapir emplacement mechanism, *Geochem. Geophys. Geosyst.,* **7,** Q05014, doi:10.1029/2005GC001185.

Weinberger, R., Begin, Z.B., Waldmann, N., Gardosh, M., Baer, G., Frumkin, A. & Wdowinski, S., 2006b. Quaternary rise of the Sedom diapir, Dead Sea basin, in *New Frontiers in Dead Sea. Paleoenviron. Res.,* Chapter 3, pp. 33–51, eds Enzel, Y., Agnon, A. & Stein, M., Geol. Soc. Am. Spec. Paper. 401, doi:10.1130/2006.2401(03).

Wells, D.L. & Coppersmith, K.J., 1994. New empirical relationships among magnitude, rupture length, rupture width, rupture area and surface displacement, *Bull. seism. Soc. Am.,* **84,** 974–1002.

Wilson, L., Sparks, R.S.J. & Walker, G.P.L., 1980. Explosive volcanic eruptions—IV The control of magma properties and conduit geometry on eruption column behavior, *Geophys. J. Roy. astron. Soc.,* **63,** 117–148.

Yılmaz, M.T., Pekcan, O. & Bakır, B.S., 2004. Undrained cyclic shear and deformation behavior of silt–clay mixtures of Adapazarı, Turkey, *Soil Dynam. Earthq. Eng.,* **24,** 497–507.

Yuan-qiang, C. & Xu, L., 2004. Dynamic properties of composite cemented clay, *J. Zhejiang Univ. Sci.,* **5**(3), 309–316.

Zak, I., 1967. The Geology of Mount Sedom, *Ph.D. thesis*. Hebrew University, Jerusalem.

APPENDIX A: VISCOSITY TESTS

Based on plasticity experiments, the natural water (brine) content of the green, clay-rich Lisan source layer is between 27 and 36 per cent (Arkin & Michaeli 1986). This water content is enough to cause a drastic loss of shear strength and flowage of the clay–water mixture during shaking (Arkin & Michaeli 1986). Levi *et al*. (2006b) suggested that the relatively low water content enabled the preservation of the magnetic fabric during the injection process. Therefore, it is assumed that not much external water was added to the fluidized source layer. This means that the amount of water during the fluidization process was probably ∼35 per cent wt. (Levi *et al*. 2006b). The measured densities of the clay-water mixture range between 1700 and 1950 kg m^{-3}.

The viscosity values and the rheology characterizations were measured by a viscometer 'Fann 35S' model at six different rates (170–1022 s^{-1}) in the Technion laboratories, Haifa. Four suspensions with different amounts of water, between 31 and 45 per cent wt, were used. Immediately after preparing the suspensions, we examined each sample to check if any possible sedimentation process occurred. For the six different rates, four best fit curves were computed. The viscosity values were calculated from the linear regression coefficients. All four rheograms indicated a linear relation between strain rate and shear stress (Fig. A1). Therefore, the rheology of the suspended mixtures of the Lisan clay-rich sediments may be well approximated by a Newtonian fluid.

The dynamic viscosity η values 0.03–0.3 Pa s correspond to the slopes of the linear regression curves. The kinematic viscosity 29×10^{-6}–15×10^{-5} m^2 s^{-1} used in eq. (4) is calculated by $\nu = \frac{\eta}{\rho_{\text{fluid}}}$.

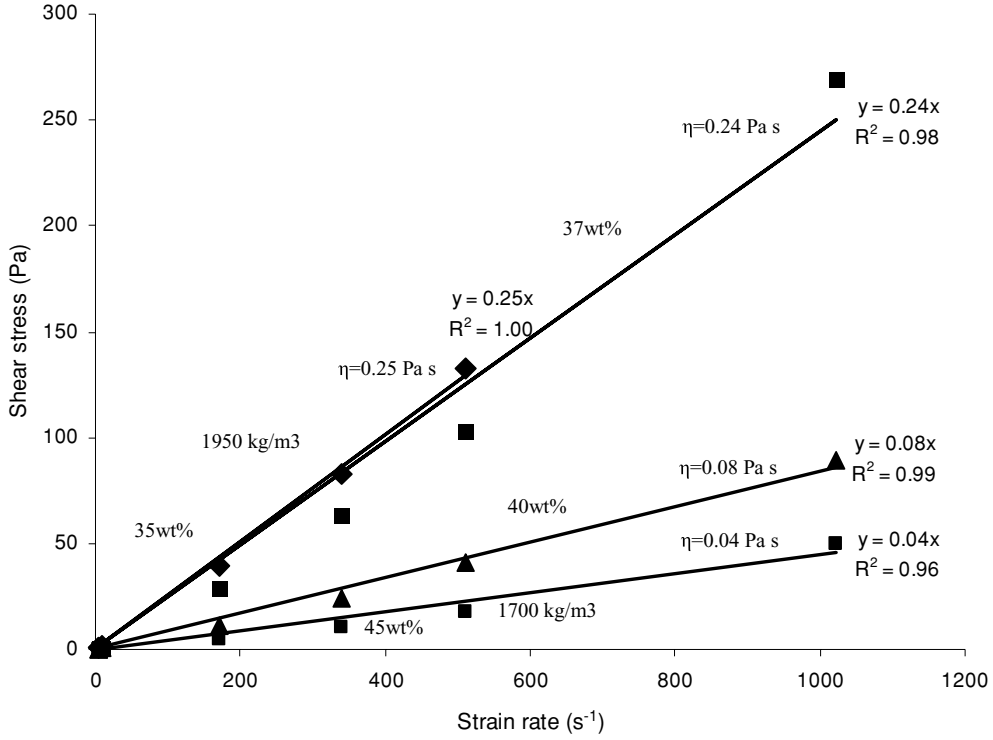

Figure A1. Results of viscosity experiments. See Appendix A for details